Uncertainty of stress path in fault stability assessment during CO₂ injection: Comparing smeaheia 3D geomechanics model with analytical approaches

Jung Chan Choi [a,*], Elin Skurtveit [a,b], Khoa D.V. Huynh [a], Lars Grande [a]

[a] *Norwegian Geotechnical Institute, Oslo, Norway*
[b] *Department of Geosciences, University of Oslo, Oslo, Norway*

ARTICLE INFO

ABSTRACT

This study investigates the limitation of simplified stress path assumptions, particularly uniaxial strain conditions, in fault stability assessments for CO₂ injection sites. We conducted a 3D geomechanics simulation for the Smeaheia fault block in the Norwegian North Sea and compared the results with simplified stress path assumptions. Our results indicate that the uniaxial strain assumption underestimates the change in effective horizontal stress, particularly for bounding faults subjected to a significant change in pore pressure gradient with soft surroundings. Rotations of maximum horizontal stresses parallel to soft surroundings are also observed along the bounding faults due to the directional difference in stiffness contrast along faults. This underestimation results in overestimation of fault stability by up to 60% for an extreme case. Our study thus highlights that the uniaxial strain assumption, which limits to account for lateral deformation on the fault/reservoir boundary, overlooks critical changes in the effective horizontal stress and associated critical scenarios for fault stability assessments. When bounding faults are juxtaposed with low-stiffness shale formation under a normal stress regime, calibrating the fault stability assessment by 30% for a base case and 60% for a conservative assessment can provide a practical way to correct the uncertainties caused by using uniaxial strain assumption.

1. Introduction

Fault-bounded structural closures have been proven as excellent traps for oil & gas in many geological settings, e.g., Troll (Horstad and Larter, 1997), indicating that these structures may also provide excellent CO₂ storage sites, as demonstrated by recent studies of the Horda Platform and Smeaheia area (Osmond et al., 2022; L. Wu et al., 2021). In order for the fault-bounded structures to provide an attractive structural CO₂ trap, it is crucial to have a good understanding of the injection-induced deformation and associated integrity issues. CO₂ injection near major bounding fault zones changes the stress acting on the faults and can increase the risk of unwanted failure or fault reactivation. If the faults are critically orientated, the fault seal capacity is primarily controlled by mechanical stability rather than the capillary trapping mechanism (e.g. Bretan et al., 2011; Streit and Hillis, 2004). Therefore, evaluating the injection-induced stress changes in faults and their associated impact on mechanical stability should be a critical aspect of the early screening process for CO2 storage sites, while capillary threshold pressure can be considered a secondary issue to be evaluated in later development phases.

Fault reactivation risk and mechanical seal integrity are mainly controlled by in-situ stresses, pore pressure conditions, mechanical properties, and injection-induced stress changes of faults. The stability level can be quantitatively represented by a safety factor or a likelihood of failure. The recent literature addressing fault integrity identifies many uncertainties and risk factors for the fault stability assessment. For the vette fault zone (VFZ) in the Smeaheia fault block, various approaches have been considered to address the failure risk. Skurtveit et al. (2018) used Mohr-Coulomb failure criteria and showed that if a cohesion above 3 MPa can be demonstrated for the faults, the most critical failure will be tensile fracturing, although not considering any horizontal total stress change during the CO₂ injection. Rahman et al. (2021) performed a probabilistic assessment of the VFZ failure risk to address the high uncertainty of the fault parameters and identified high sensitivity for the fault strength properties as well as the stress conditions. Michie et al. (2021) tried to quantify the uncertainty related to the fault-picking strategy and highlighted implications for further stability assessments. Although the main messages of the studies are that the risk of failure is low, there is still a need for a better understanding of the injection-induced stress change in the bounding faults of structural traps, as this provides essential input for any fault stability assessment.

Nomenclature

C_0	cohesion
C_{ijkl}	constitutive matrix
K_0	in-situ effective stress ratio, σ_h'/σ_v'
ε_{ij}^e	Elastic strain tensor
ε_{ij}^p	Plastic strain tensor
μ'	effective friction coefficient
μ'_{mob}	mobilized friction coefficient
ν'	drained Poisson's ratio
$\sigma'_{h,initial}$	in-situ horizontal effective stress before the injection
σ_H	In-situ maximum horizontal stress
σ_h	In-situ minimum stress
σ_h'	effective horizontal stress
$\sigma'_{n,\ fault}$	Effective normal stress acting on fault
σ_v	In-situ vertical stress
σ_v'	effective vertical stress
$\sigma'_{v,initial}$	in-situ vertical effective stress before the injection
τ_{fault}	Shear stress acting on fault
P_c	allowable injection pressure
$\gamma'_{h,uniaxial}$	horizontal effective stress path coefficient considering uniaxial strain condition
γ'_h	horizontal effective stress path coefficient
$\gamma'_{v,uniaxial}$	vertical effective stress path coefficient considering uniaxial strain condition
γ'_v	vertical effective stress path coefficient
τ_{mob}	mobilized shear strength
C3D8RP	8-node trilinear displacement and pore pressure element with reduced integration
D	Dip
DOF	degrees of freedom
E	Young's modulus
FE	Finite element
IR	Intra reservoir faults
MSL	mean sea level
NB	northern bounding faults
ØFC	Øygarden Fault Complex
P25	25th percentiles
P50	50th percentiles
P75	75th percentiles
PP	In-situ pore pressure
S	Strike
SD	Standard deviation
TVD	True vertical depth
VFZ	Vette Fault Zone
α	Biot's coefficient
γ	total reservoir stress path
δ	Kronecker delta
θ	fault dip angle

The complexity level of the fault stability assessment or screening methods largely depends on the level of accuracy of the injection-induced stress changes acting on the faults and associated strength variation. Fault stability assessment is mainly carried out by comparing the stress condition acting on the fault plane to its strengths. In early studies, the injection-induced fault stress change was commonly assumed to be the same as the pore pressure change (Streit and Hillis, 2004). This simplified assumption provides a straightforward way to estimate the injection-induced stress change on faults but may not always hold true unless the rock is already at failure. Moreover, the assumption does not include any poroelastic effects affecting the total horizontal stress change (Fjær et al., 2008). If the total horizontal stress changes due to poroelastic effects during injection are not properly considered, the resulting fault stability analysis can be conservative and provide a lower allowable injection pressure (Rutqvist et al., 2007). van den Bogert and van Eijs (2020) also pointed out from a geometrical point of view that Mohr-circle evaluations provide a non-conservative estimate of the allowable reservoir pressure in cases where the reservoir is offset by a fault. Uniaxial strain assumption is thus the most widely used way to consider the poroelastic effect. The uniaxial strain condition assumes no lateral displacement and unrestricted vertical movement during the deformation. This uniaxial strain assumption has been widely used to estimate reservoir depletion or injection-induced geomechanical behaviour. Particularly for a laterally extended reservoir with relatively homogenous material and pore pressure distribution, the uniaxial strain condition is known as a good approximation of geomechanical behaviour at the centre of a reservoir (Fjær et al., 2008; Søreide et al., 2014). However, the applicability at a periphery of the reservoir or a bounding fault has not been well validated (Cuisiat et al., 2010). Particularly, the effects of reservoir heterogeneity in material properties and pore pressures on the stress paths of bounding faults need more understanding.

The numerical models or semi-analytical solutions could also be used for fault stability assessment with complex geometries (e.g., Rutqvist et al., 2013; Soltanzadeh and Hawkes, 2008). CO_2 injection-induced stress change and related deformation can be well simulated through geomechanical analysis (e.g., Bjørnarå et al., 2014; Rahman et al., 2022; Rutqvist, 2012). Especially, a 3D reservoir geomechanics model can provide an overview of mechanical status before field operations (e.g. in-situ stress conditions) as well as field operation (e.g., oil and gas depletion, CO_2 injection, drilling, etc.) induced mechanical responses (e. g. stress change, deformation, mechanical failure, and the associated change in hydraulic and petrophysical properties). Such a numerical model can also capture both effects of pore pressure (poroelasticity) and temperature (thermo-elasticity) on mechanical behaviour (e.g., Thompson et al., 2021). Rahman et al. (2022) illustrate the need to populate the heterogeneous material models with relevant parameters using a seismic data-driven 3D field-scale geomechanical model by highlighting the effect of the detailed seismically interpreted inputs on the geomechanical behaviours. Rutqvist et al. (2007) indicate that simplified analytical techniques may underestimate or overestimate the maximum sustainable injection pressure and emphasize the importance of a numerical model for field stability assessment.

Despite the benefits of using the numerical model for the fault stability assessment, making a 3D geomechanics model in an early stage of field development is challenging. A successful 3D geomechanical model requires a detailed geological model describing the 3D geometry of the reservoir, fault zones and the over- and under-burden. Furthermore, relevant geomechanical properties describing the elastoplastic properties and stress conditions are needed. However, there is often only limited information on rock mechanical data, stress field, and fault characterization in an early project phase. Thus, the early screenings have to be carried out by only a simplified analytical solution with certain assumptions on the stress change acting on the faults rather than field-scale 3D or 4D numerical modelling approaches. Most screening studies based on analytical approaches should somewhat rely on simplified assumptions. Thus, one of the keys to a successful early-phase screening of critically orientated faults might be a better understanding of the injection-induced stress change of faults and quantifying associated uncertainties caused by the simplified model assumptions.

In this study, we assess the impact of the simplified stress path

assumptions, particularly uniaxial strain condition, on fault stability assessment for CO2 storage sties. We conduct 3D geomechanical simulation for the Smeaheia fault block in the Horda Platform to calculate injection-induced stress changes during CO_2 injection. By comparing the numerically simulated spatial distribution of horizontal and vertical effective stress changes with a simplified estimation assuming uniaxial strain conditions, we identify the limitation of the uniaxial strain condition and its effect on fault stability assessments. Finally, we discuss the implications of our findings for CO2 storage projects in the Norwegian Continental Shelf.

2. Fault stability assessment

Faults can be reactivated when the stresses acting on the fault exceed its strengths. Thus, the fault stability can be evaluated by comparing the stresses acting on the fault plane to its frictional strength, which can be defined by various failure criteria (e.g., Mohr-Coulomb criteria). In porous rock, failure is associated with the stress acting on the rock frame, known as effective stress (Terzaghi, 1943). The effective stress σ' used for this study can thus be defined as the total stress σ minus the pore pressure p_p, given by $\sigma' = \sigma - p_p$. Assuming the principal stress directions are aligned with Cartesian stresses direction (σ_v, σ_H, σ_h), the effective stresses acting on the faults can be estimated by mathematical decomposition of the stress condition around faults (σ_v, σ_H, σ_h, and pore pressure) using the fault geometry (dip and strike) (Wiprut and Zoback, 2002). For example, considering isotropic horizontal stress conditions under a normal faulting regime, the effective normal stress $\sigma'_{n,\ fault}$ and shear stress acting on the fault τ_{fault} can be expressed as:

$$\sigma'_{n,\ fault} = \frac{\sigma'_v - \sigma'_h}{2} + \frac{\sigma'_v + \sigma'_h}{2} cos2\theta \tag{2.1}$$

$$\tau_{fault} = \frac{\sigma'_v - \sigma'_h}{2} sin2\theta \tag{2.2}$$

where σ'_v and σ'_h are effective vertical and horizontal stresses, respectively. The θ is the fault dip angle. It is noted that our study area Smeaheia is expected to have a normal faulting regime and close to isotropic horizontal stresses (Andrews et al., 2016; Thompson et al., 2022). However, in order to consider the injection-induced horizontal stress anisotropy, this study uses full 3D stress decomposition.

The distance from the decomposed stresses acting on the fault plane ($\sigma'_{n,fault}$ and τ_{fault}) to the strength criteria or failure envelope can be a measure for stability evaluation (Fig. 1). There are many different ways to define the distance (or relative distance) between the stress and the strength (failure criteria). The failure criteria could also be defined by different failure mechanisms, including shear and tensile failure. According to Skurtveit et al. (2018), when the fault cohesion is higher than

the maximum shear stress of faults, the study reported that the fault failure could be mainly governed by a tensile failure. However, there are high uncertainties in the fault strength, especially for cohesion, because the strength parameters of faults can be governed mainly by their geometrical irregularity (e.g., roughness, throw direction, etc.) rather than a thin gauge from surroundings intact rocks (Barton and Bandis, 1991; Marone, 1995). It is thus commonly assumed that faults have a lower cohesion than surroundings, and the associated main failure mechanism can consequently be a shear failure. Thus, we mainly focus on the instability caused by the shear failure. In this study, the mobilized shear strength τ_{mob} is mainly used to quantify fault stability. In addition, allowable injection pressure P_c, which is commonly used to assess a margin for additional pressure increase near faults, is also compared to the mobilized shear strength. The conceptual meaning of stability measure τ_{mob} and P_c is illustrated in Fig. 1 using the Mohr circle diagram and a coulomb failure envelope.

The mobilized shear strength τ_{mob} is defined as the ratio of the mobilized shear stress to its maximum resistance or strength, particularly to its friction coefficient. When the fault is stressed by its surrounding, the shear stress acting on the faults can increase only until its maximum possible resistance, which is shear strength. As the shear stress increases, the mobilized shear strength can thus reach to maximum 1.0. In geotechnical and structural engineering, the mobilized shear strength is widely used as a measure for stability evaluation that can show the relative distance between the stress and the strength (Ching and Phoon, 2013; Mesri and Shahien, 2003; Wong et al., 2007). The mobilized shear strength can be defined as:

$$\tau_{mob} = \frac{\mu'_{mob}}{\mu'} = \frac{\left[\dfrac{\tau_{fault}}{\frac{C_0}{\mu'} + \sigma'_{n,fault}}\right]}{\mu'} \tag{2.3}$$

where μ'_{mob} is mobilized friction coefficient, C_0 is the cohesion, and μ' is the effective friction coefficient. For the cohesionless case, where $C_0 = 0$, the mobilized friction coefficient becomes the same as the slip tendency (ratio of shear stress to normal stress) (Morris et al., 1996).

The allowable injection pressure P_c, which is also known as critical pressure perturbation (Wiprut and Zoback, 2002), represents the change in pore pressure ΔP that triggers a shear failure. The P_c can be defined as a horizontal distance between the stress acting on the faults and the failure envelope. Since it underestimates the allowable injection pressure due to its simplified stress path during the injection, which is a horizontal distance, it is often used as a conservative evaluation. The P_c equation is expressed as follows:

$$P_c = \sigma'_{n,fault} - \frac{\tau_{fault} - C_0}{\tau'} \tag{2.4}$$

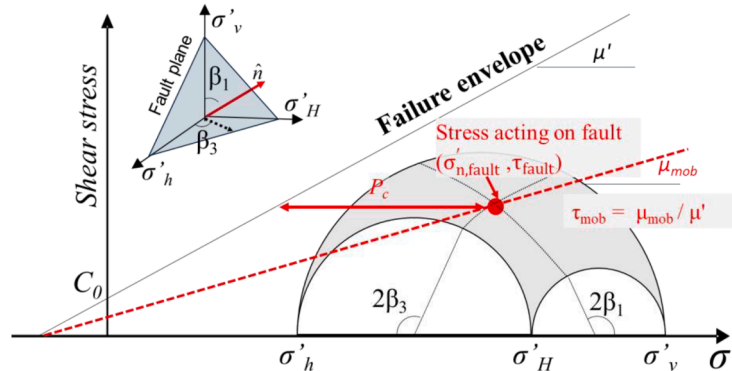**Fig. 1.** Conceptual meaning of mobilized shear strength (τ_{mob}) and allowable injection pressure (P_c), illustrated in the 3-D Mohr circle diagram. The symbols in the figure are defined in the text. Note: the principal stress directions are assumed to follow the geological stresses σ_v, σ_H, σ_h under a normal faulting regime.

2.1. Injection-induced stress changes around bounding faults

During the injection, increased pore pressure reduces the in-situ effective principal stresses, and the fault stress condition becomes closer to the failure envelope. Consequently, the fault stability is reduced. Thus, it is very important to estimate the change of effective stress correctly. Regarding the effective stress concept used for the stability assessment, it is important to note that effective stress should be defined by a general Terzaghi concept where $\sigma' = \sigma - p_p$, rather than Biot's effective stress concept with Biot's coefficient α where $\sigma' = \sigma - \alpha p_p$. While Biot's effective stress is only applicable and valid for a poroelastic deformation caused by external stresses and the pore pressure change, the Mohr-Coulomb criteria is an empirical correlation measured based on Terzaghi's effective stress condition. Thus, Terzaghi's concept is the more relevant definition for the failure criteria (Detournay and Cheng, 1988; Fjær et al., 2008; Gueguen and Bouteca, 1999).

To quantify the effects of pore pressure change on the stress evolution, the change of total vertical and horizontal stresses ($\Delta\sigma_v$ and $\Delta\sigma_h$) caused by pore pressure change ΔPP can be expressed using vertical and horizontal stress path coefficients γ_v and γ_h (Hettema et al., 2000):

$$\gamma_v = \frac{\Delta\sigma_v}{\Delta PP} \tag{2.5}$$

$$\gamma_h = \frac{\Delta\sigma_h}{\Delta PP} \tag{2.6}$$

As our study focuses on the relationship between pore pressure and effective stresses, and their impact on stability assessment, it may be more straightforward to use effective stress path coefficients. If the relationship between effective stresses and pore pressure changes is defined by total stress path coefficients, effective stress path coefficient γ' can be expressed using total reservoir stress path coefficient γ and Biot's coefficient α as follows:

$$\gamma' = \gamma - \alpha \tag{2.7}$$

Then, the vertical and horizontal effective stresses after the injection can be defined as:

$$\sigma_v' = \sigma_{v,initial}' + \gamma_v'\Delta PP \tag{2.8}$$

$$\sigma_h' = \sigma_{h,initial}' + \gamma_h'\Delta PP \tag{2.9}$$

where $\sigma_{h,initial}'$ and $\sigma_{v,initial}'$ are the in-situ horizontal and vertical effective stresses before the injection, respectively.

Assuming that the pore pressure does not affect the change in total stresses, which means that the stress path coefficients in Eqs. (2.5) and (2.6) can be 0.0, the effective stress paths defined in Eq. (2.7) can be $\gamma_v' = \gamma_h' = -1.0$ with an assumption of $\alpha = 1$. It assumes that the pore pressure is the only factor affecting the change of the effective stresses. For a normal faulting regime ($\sigma_v > \sigma_h$), when the injection-induced effective vertical stress σ_v' and the effective horizontal stress σ_h' assuming no change in total stress, Eqs. (2.8) and (2.9) are expressed as:

$$\sigma_v' = \sigma_{v,initial}' - \Delta PP \tag{2.10}$$

$$\sigma_h' = \sigma_{h,initial}' - \Delta PP \tag{2.11}$$

However, injection-induced change of in-situ stress conditions around faults is affected by other factors (e.g., boundary condition, reservoir geometry, material properties, etc.), and the effective horizontal stress path coefficients will normally be less negative than -1.0. Thus, the uniaxial strain condition is a more commonly used assumption for a reservoir stress path (Fjær et al., 2008). The uniaxial strain condition assumption is considered valid for the middle of a laterally extensive reservoir with homogenous material properties. The uniaxial strain condition assumes negligible lateral and unconstrained vertical movement. In such uniaxial strain conditions, the effective stress path coefficients in Eq. (2.7) can be expressed:

$$\gamma_v' = -\alpha \tag{2.12}$$

$$\gamma_h' = \gamma_h - \alpha = \frac{\alpha(1 - 2\nu')}{1 - \nu'} - \alpha \tag{2.13}$$

where ν' is the drained Poisson's ratio, and α is the Biot's coefficient.

For unconsolidated rock where the drained bulk modulus is several orders of magnitude smaller than its grain-level bulk modulus, the Biot's coefficient is close to 1.0 and set to 1.0 in this study on poorly consolidated sedimentary rocks. When Biot's coefficient is set to 1.0, Eq. (2.13) can be rewritten as:

$$\gamma_h' = \frac{-\nu'}{1 - \nu'} \tag{2.14}$$

As the Poisson's ratio can be in the range of 0.0–0.5 for various materials, the γ_h' representing uniaxial strain condition in Eq. (2.14) could theoretically vary in the range of 0.0–-1.0. However, most sandstones have a Poisson's ratio in the range of 0.1–0.3 and the corresponding γ_h' by using Eq. (2.14) are then in the range of around -0.1 to -0.4. Then in practice, γ_h' used in the analytical model may be in the range of -0.1 to-1.0 based on the two main assumptions used in the analytical model in Eqs. (2.11) and (2.14), respectively. The vertical effective stress path γ_v' under both assumptions for analytical solution equals -1.0. However, in reality, it could be less or larger when accounting for deformation, like arching effects. In addition, the effective stress anisotropy can develop differently with the uniaxial strain assumptions and affect the calculated stability. To perform a detailed study of the injection-induced stress changes around the bounding fault of the Smeaheia fault block, 3D numerical geomechanical models are used to investigate the spatial distribution of effective stress change around the bounding faults. The 3D geomechanical models can capture the effects of geometry or location in the reservoir (Rudnicki, 1999), depth of the reservoir (Hettema et al., 2002), and stiffness contrast (Morita et al., 1989), which are aspects that become important for the bounding faults. Comparing the effective stress paths estimated using the 3D geomechanical models and the analytical model using uniaxial strain conditions demonstrate the validity of the analytical methods for fault stability screening.

2.2. 3D geomechanics modelling

In the reservoir, pore pressure change influences the stress on the grain skeleton (effective stress) and the total stress. The total stress tensor can thus be decomposed by the effective stress tensor σ_{ij}' and pore pressure p_p as follows (Terzaghi, 1943):

$$\sigma_{ij}' = \sigma_{ij} + p_p\delta_{ij} \tag{2.15}$$

where δ is the Kronecker delta. The strain ε_{ij} caused by the effective stress change can be decomposed by an elastic part ε_{ij}^e and a plastic part ε_{ij}^p as follows:

$$\varepsilon_{ij} = \varepsilon_{ij}^e + \varepsilon_{ij}^p \tag{2.16}$$

The relationship between the effective stresses and the elastic strain can be linked with the constitutive matrix C_{ijkl} as follows (Rice, 1977; Suvorov and Selvadurai, 2019):

$$\sigma_{ij}' = C_{ijkl}(\varepsilon_{kl} - \varepsilon_{kl}^p) + (1 - \alpha)p_p \tag{2.17}$$

where α is the Biot's coefficient which is related to the compressibility of the formation grain.

The 3D geomechanics model needs several steps together with the multidisciplinary data (e.g. geological model, geometry, 3D impedance cube from seismic information, petrophysical data and pore pressure from a reservoir simulator, etc.). This study uses a general-purpose finite element (FE) solver Abaqus 2017 (Dassault Systèmes Simulia Corp, 2017) to solve the constitutive relationships between the reservoir pressure and the stress and strain of discretized geometry of the CO_2 storage, which are expressed in Eqs. (2.15) to (2.17). In addition, an NGI's in-house Python scripts and Fortran user subroutines to import the multidisciplinary data are used (Choi et al., 2019). The material behaviour of the field was modelled using a linear elastic perfectly-plastic Mohr-Coulomb model. The reservoir section was considered a drained material, and the sections outside the reservoir were considered undrained. The model mesh used C3D8RP (8-node trilinear displacement and pore pressure element with reduced integration) was used to consider the effect of pore pressure and stress

changes. Reservoir geometry and main geological horizons were imported using the geometrical information from the published geological and reservoir model (Gassnova 2021). Our model considered a spatial variation of the material properties when the 3D data was available. For the reservoir, the variations in the drained elastic stiffness as a function of porosity were modelled by a user-defined field parameter, where the initial field parameter distribution is taken equal to the distribution of the initial porosity in the reservoir. The initial effective stresses and pore pressures were assumed to be in equilibrium with the total stresses generated by gravity and tectonic forces. To generate the initial stress equilibrium without causing initial deformation, nodal reaction forces were first calculated by fully constraining all displacement degrees of freedom (DOF). Then, the calculated nodal reaction forces were applied to the model with gravity and tectonic forces. Next, the CO_2 injection-induced pore pressure changes simulated separately from a reservoir simulator were applied to the pore pressure nodes of the
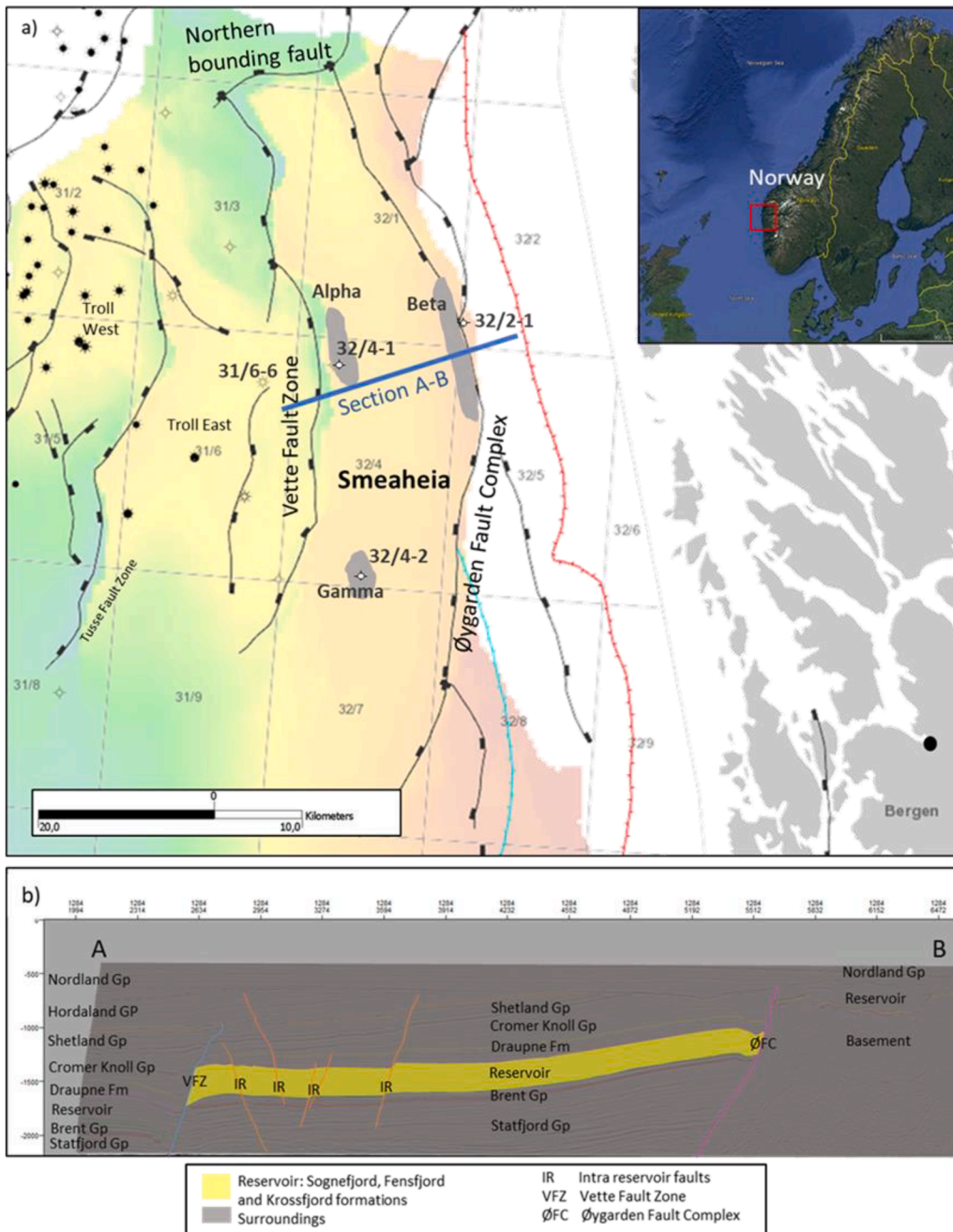
Fig. 2. a) Location and extent of the Sognefjord Formation and the Smeaheia fault block on the Horda Platform showing three potential closures for CO_2 storage, the Alpha, Beta and Gamma. b) Profile across Smeaheia with the Sognefjord, Fensfjord and Krossfjord formations grouped as the reservoir and the overburden, underburden and sides grouped as the surroundings. Location of the intra-reservoir faults (IR) and two main bounding faults, the Vette Fault Zone (VFZ) and the Øygarden Fault Complex (ØFC) are included. The map is based on NPD FactPage data, and the profile is based on interpretation by Mulrooney et al. (2020).

reservoir section to calculate the mechanical response caused by the field operation. Finally, the calculated mechanical responses were exported as an independently processible format (e.g., ASCII or binary).

3. Study area and model properties

3.1. Smeaheia study area

The Smeaheia fault block is located on the eastern part of the Horda Platform offshore Norway, part of the north-south-trending structural high on the eastern side of the Viking Graben (Fig. 2a). The tectono-stratigraphic evolution for the Smeaheia area is well described in recent publications (Mulrooney et al., 2020; Osmond et al., 2022; L. Wu et al., 2021), identifying two major extensional rift events, as well as uplift. The stratigraphic succession of the Smeaheia fault block can be described based on the three dry wells targeting identified structural traps, the Alpha, Beta and Gamma (Fig. 2a). The structural traps within Sognefjord Formation are identified as a promising CO_2 storage reservoir within the Upper Jurassic Viking Group (Gassnova, 2021) and capped by the sealing Draupne Formation (Skurtveit et al., 2012). The Sognefjord, Fensfjord and Krossfjord formations are considered the main reservoir succession modelled in the 3D geomechanical model, whereas all other formations are considered surrounding material (Fig. 2b). A reference dataset containing subsurface data, reports, geomodels and reservoir simulations for the assessments of CO_2 storage sites in the Smeaheia region has been published by Gassnova and Equinor through the CO2datashare database (https://co2datashare.org/dataset/smeaheia-dataset) (Gassnova, 2021) and provides the base for the current modelling. The released Smeaheia Dataset covers the period from 2009 to 2018, whereas the latest well 32/4–3S drilled in the Gamma closure (Gladsheim) is not included in the Smeaheia dataset.

Smeaheia is a fault-bounded structure to the east, north and west, whereas the structure is open to the south (Fig. 2a). The Vette Fault Zone (VFZ), bounding the Alpha closure to the west, is a north-south trending, west-dipping normal fault with a prominent wedge-shaped growth section during the deposition of the Cromer Knoll Group. A comparison of the lithology and geometry of the Alpha closure and the similar trap structures within Troll east and west suggests that the Cromer Knoll Group is expected to act as a good horizontal seal along the Vette Fault Zone, whereas within the identified relay zones, fault segmentation results in reservoir-reservoir contact across the Vette Fault Zone with potential for pressure communication (Mulrooney et al., 2020; Wu et al., 2021). To the east, the Smeaheia fault block is bounded by the Øygarden Fault Complex (ØFC), which is the boundary of the sedimentary basin and the Precambrian basement rock of the Norwegian mainland (Fossen et al., 2017). The basement rock of the Øygarden Fault Complex is currently not well known with respect to fault sealing and stiffness properties.

3.2. Model inputs

The geomechanical models in our study consist of two different mechanical material types: the reservoir section and the surrounding material (Fig. 2b). The geometry of the model is based on the nine seismic horizons interpreted in the Troll Kystnær storage prospect between 2009 and 2012 by Gassnova (Gassnova, 2021), but available geomechanical data only supported two distinct geomechanical layers. The Sognefjord, Fensfjord and Krossfjord formations were grouped as the reservoir section, and all other layers were defined as surrounding materials. Each material type has been assigned based on the available data from the Smeaheia dataset (Gassnova 2021) and supplemented with input from recent publications (Table 1). To consider the effect of material heterogeneity on the reservoir stress path, we used porosity distribution from the geomodel provided in the Smeaheia dataset and a correlation between Young's modulus and porosity established from relevant data reported by Mondol (2019) and Park et al. (2022). Park

Table 1

Mechanical properties used for the 3D geomechanics modelling study based on Gassnova (2021), Mondol et al. (2019), Grande et al. (2020), and Park et al. (2022).

Properties	Unit	Value
Reservoir		
Drained Young's modulus	GPa	$36.97–9.66*\log_{10}(\text{porosity}[1][-]*100)$
Drained Poisson's ratio	–	0.22
Cohesion	MPa	5.00
Friction angle	°	15.00
Surroundings, including over- and under-burden		
Undrained Young's modulus	GPa	5.00
Undrained Poisson's ratio	–	0.40
Cohesion	MPa	7.00
Friction angle	°	13.00

[1] porosity = V_{pore} / V_{bulk}.

et al. (2022) presented a sample from the Sognefjord Formation in well 31/6–6 (Fig. 2a) with 28% porosity and Young's modulus, *E*, of 2.0 and 5.2 GPa during triaxial loading and unloading, respectively. The Sognefjord Formation in well 32/4–1 (Fig. 2a) has an average porosity of 30% and a range of 25–35% (Mondol, 2019), corresponding to Young's modulus in the range of around 1–6 GPa. The average of the porosity-dependant Young's modulus used for this study is 5.56 GPa, which is close to the unloading modulus because the injection-induced pressure unload the reservoir materials. However, the caprock and the surrounding could also be stressed due to a counter force caused by the expansion of the reservoir if negligible fluid infiltration to the surroundings is assumed. Thus, the variations of surrounding stiffness are also investigated in the parametric study. The Biot's coefficient for all materials is set to 1.0 based on the assumption that the drained bulk modulus is several orders of magnitude times smaller than its grain-level bulk modulus for the Horda Platform area. Poisson's ratio is a critical input in estimating the effective horizontal stress path γ'_h using the uniaxial strain assumption (Eq. 2.14), and its variation can affect the distribution of stress paths in the reservoir and surrounding areas. To exclude the difference caused by the variation in Poisson's ratio in the stress paths between analytical and numerical simulations, a constant Poisson's ratio of 0.22 was selected for the reservoir and 0.4 for the surrounding areas was chosen based on the range tabulated in the Smeaheia dataset. The strength parameters, including the cohesion and the friction angles, are also derived from the Smeaheia dataset. The friction angle for the reservoir section, which is 15.0 °, is slightly lower than the typical range for the reservoir sandstones, which varies between 20 and 40 °. Friction angles tend to decrease with higher confining stresses and increasing porosity (Fjær et al., 2008), but the database does not clearly comment on it. In addition, there are high uncertainties in the fault strength, especially for cohesion, and the cohesion of faults is commonly assumed to be lower than the surroundings. To investigate the effect of variation in strengths on the stability assessment results, we chose the intact rock properties ($C_0 = 5$ MPa, $\mu' = 0.27$, which corresponds to 15° of the effective frictional angle) as a high-value case for the fault strengths and cohesionless faults ($C_0 = 0.0$ MPa, $\mu' = 0.6$) as a low-end of the fault strengths for the fault stability assessment study.

In the model, effective unit weights are assumed to be 10.235 kPa/m, and the initial pore pressure is assumed to follow a hydrostatic pore pressure, although the recent well drilled in the Gamma closure confirmed depletion on the Smeaheia fault block (L. Wu et al., 2021). A fixed value of in-situ effective stress ratio $K_0 = \sigma_h'/\sigma_v' = 0.45$ is applied for all lithologies, although K_0 may vary between 0.4–0.8 for various lithologies as observed from field stress data (Andrews et al., 2016; Andrews and de Lesquen, 2019; Thompson et al., 2022). Thompson et al. (2022) reported that the study area has some degree of horizontal stress anisotropy ($\sigma_H/\sigma_h = 1.01 - 1.27$), and the primary orientation of

the maximum horizontal stress is the E-W direction. This study assumes an isotropic horizontal stress condition as the initial horizontal anisotropy condition but investigates the development of injection-induced horizontal stress anisotropy. The depths of the injection point and the top reservoir are set to 1488 and 1304 m TVD MSL, respectively.

A parametric study has been conducted to evaluate the sensitivity of soft and stiff material surrounding the reservoir. A Young's modulus of 2.0 GPa is considered to represent soft material, typically a weaker or very clay-rich formation surrounding the reservoir, whereas Young's modulus of 7.0 GPa, is used to study the effect of a stiffer material surrounding the reservoir (Table 2). The range of the stiffness is based on the depth variation of static Young's modulus as well as the non-linear behaviour of representative surrounding shales like the Nordland Group, Southern Viking Graben and the Draupne shale from well 16/8–3S during shear mobilization (i.e., Grande et al., 2020). It also reflects variation in anisotropy (i.e. $E = 2.5$–5 GPa normal and parallel to layering for Draupne Shale from Ling Depression) (Mondol, 2019). Regarding the choice of loading direction, as pressures increase in the reservoir, the material experiences elastic unloading. However, the caprock and bounding materials, which have negligibly small fluid infiltration, may also be stressed/loaded due to a counterforce caused by the expansion of the reservoir. Consequently, we have selected ranges that can accommodate both loading and unloading stiffness.

Fault geometry interpreted in the Troll Kystnær report (Gassnova, 2013) is used as a base for this study. The faults around the reservoir are plotted in Fig. 3. The reservoir is bounded by three main fault systems: VFZ (west), ØFC (east), and the northern-bounding (north) fault zones. The N-S to NNW-SSE orientated VFZ and ØFC make up the western and eastern boundaries of the Smeaheia fault block, a roughly E-W trending fault system bound to the north, whereas the reservoir is open to the south (Figs. 2a and Fig. 3). Faults within the reservoir are mainly NW-SE trending, and only a selection of faults are part of the current model. The statistical distribution of fault strikes, mean values and standard deviations (SDs) for the various fault systems are summarized in Fig. 4. Assessment of fault dip depends on the velocity model used for depth conversion of the seismic data. Michie et al. (2021) observed shallow dipping faults around 35° in the upper section of the Vette Fault Zone, steepening towards around 70° before becoming shallower at the base. Based on the fault interpretation published by Michie et al. (2021), we consider a fault dip of 60° and a fault strike of 169° as representative values for further consideration of fault stability evaluation. For a sensitivity study, a fault dip of 42° is also considered based on other interpretations (Rahman et al., 2021; Skurtveit et al., 2018). In addition to the base strike, another strike of 252° is also tested to investigate the effect of injection-induced horizontal stress anisotropy. The representative faults for the stability assessments are assumed to be located near the injector, which has a depth of around 1400 m below MSL. Corresponding in-situ vertical and horizontal total stress, conditions are 25.6, 18.7, and pore pressure is 13.9 MPa. The pore pressure build-up near the injector is assumed to be 3.4 MPa.

The reservoir simulation by Equinor for the 2016 feasibility study

(Gassnova, 2021) was used to consider the 3D distribution of injection-induced pore pressure build-up in the reservoir. The model simulated 1.3 million tonnes of yearly injection for 25 years. The simulation model assumed a closed boundary for the northern, eastern and western bounding faults and opened boundary for the intra-faults. The simulation also assumed the side burden juxtaposed with bounding faults as a hydraulically closed boundary condition. The different assumptions on the hydraulic boundary condition of the fault can also affect the results of specific site evaluations. Since this study aims to investigate a more general conclusion about the effect of analytical approaches assumption by using field case, we kept the assumption used in the reservoir simulation. It should be noted that the results using this assumption may not reflect the site-specific operational condition, and the detailed field assessment is out of the scope of this study. The pore pressure distribution in the reservoir after 25 years of injection (Fig. 5a) shows a pore pressure increase of up to 3.4 MPa near the injector. The northern part of the reservoir has pressure close to that near injector due to the closed boundary condition at the northern bounding fault. The pore pressure is gradually decreasing from the injector to the southern open boundary.
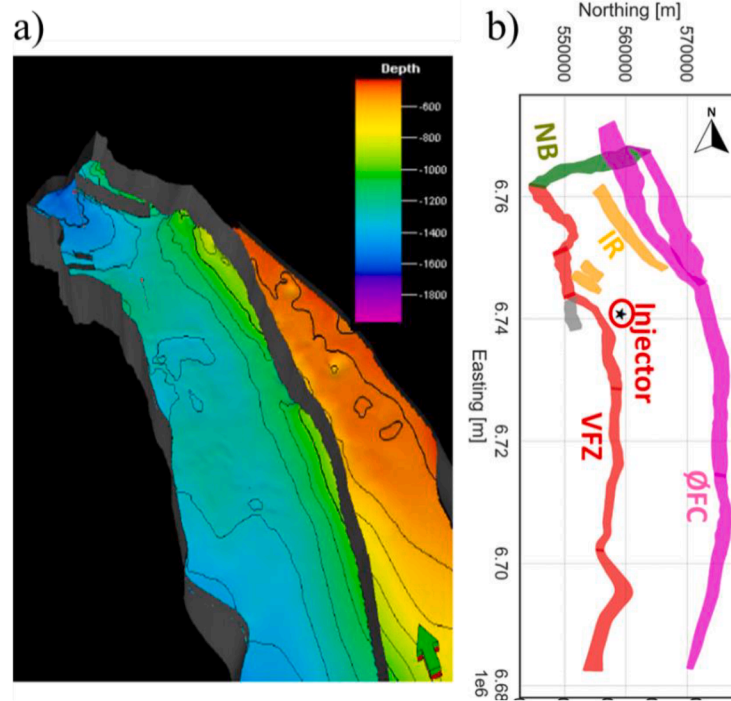
4. Results

4.1. Stress change simulated from 3D geomechanics model

The generated 3D model has width, length, and height of 30.5, 83.4, and 5.0 km, respectively (Fig. 6a), with a total number of elements of the reservoir and the entire model of $1.9 \bullet 10^5$ and $4.3 \bullet 10^5$, respectively. The total number of grids in the vertical direction is 31. The change of vertical effective stress (Fig. 6b) follows the pore pressure change (Fig. 6a) in terms of both distribution (i.e., higher change near the injector and gradually reducing toward the southern boundary) and the magnitude. For the effective vertical stresses (Fig. 6b), the injection-induced pore pressure change appears to be the major factor affecting the change of vertical effective stresses (Eqs. 2.10 and 2.12), and simplified assumptions seem to be acceptable for overall behaviour. However, for the horizontal effective stresses, the change in horizontal effective stress (Fig. 6c) is much smaller ($< \sim40$ per cent of pore pressure change) compared to pore pressure (Fig. 6a). The smaller change in horizontal effective stress (Fig. 6c) than in pore pressures indicates that the simplified assumption in Eq. (2.11), which assumes that pore pressure is the only factor changing effective stresses, may lead to an overestimation of the change in effective horizontal stresses.

4.2. Spatial distribution of effective stress paths

Effective stress path coefficients, defined as the normalized change of effective stress by the change of pore pressure (Eqs. 2.5, 2.6 and 2.7), are used to characterize the spatial distribution of stress changes in the reservoir and along faults (Fig. 7). The simulated vertical effective stress path coefficients γ'_v are close to -1.0 for most regions in the reservoir (Fig. 7a). However, the region close to the reservoir's edge shows slightly less negative and higher variation than the reservoir. In general, the simulated values seem to follow a normal distribution with a mean of -1.0 (Fig. 7b). However, the bounding faults (i.e., VFZ, ØFC, and NB) show slightly less negative histogram peaks ($\sim$0.90–0.96) than those in the reservoirs (i.e., IR). The variation of vertical effective stress path coefficients in the bounding faults group (SD of 6–7%) is slightly higher than that in the reservoir (SD of 3–4%). The vertical effective stress path coefficient is related to the overburden arching effect, indicating how much reservoir compaction is affected by over- and side-burden support. It is noted that the arching coefficient defined by Hettema et al. (2000) uses the ratio of total vertical stresses to pore pressure defined in Eq. (2.5), and it can be converted to the effective stress path coefficients using Eq. (2.7). If the vertical movement of the reservoir is not confined

Table 2
Parametric cases used to investigate the sensitivity of stiffness distribution and contrast on the effective stress paths.

NO.	Cases	Young's modulus in reservoir, E_reservoir [GPa]	Young's modulus in reservoir surrounding, E_surrounding [GPa]
0	**Base**	**Inhomogeneous, Mean = 5.56**	**5.0**
1	Constant E_res	**Homogeneous, 5.56**	5.0
2a	High_E_sur	Inhomogeneous, Mean = 5.56	**7.0**
2b	Low_E_sur	Inhomogeneous, Mean = 5.56	**2.0**

Fig. 3. a) Fault planes together with depth of the top Sognefjord Formation horizon and b) top view of the fault groups used for this study; VFZ: Vette Fault Zone, ØFC: Øygarden Fault Complex, NB: northern bounding faults, IR: intra reservoir faults.

Fault groups	Strike (°)	
	Mean	SD
ØFC	168.7	19.2
NB	252.0	12.4
IR	249.6	78.9
VFZ	169.5	29.2
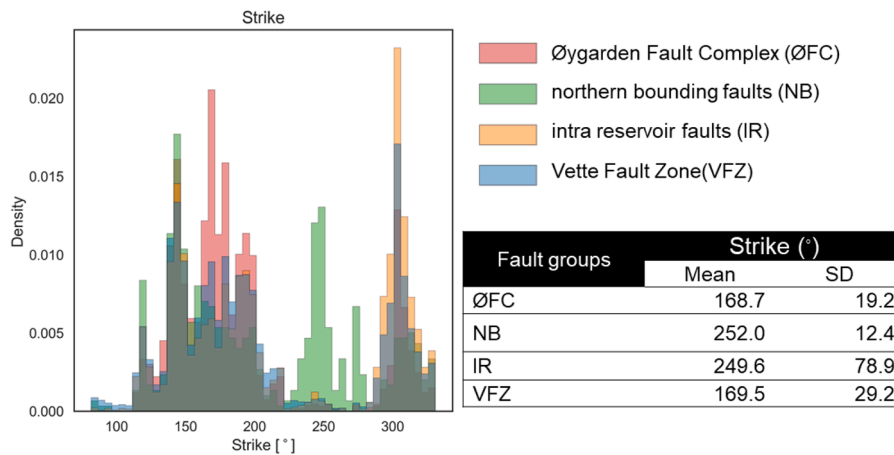
Fig. 4. Histogram and statistical mean and standard deviation of strikes of the fault used in the model.

(e.g., free moving), this effective vertical stress path coefficient is close to -1.0. Also, the uniaxial strain condition assumes the vertical movement to be under a free boundary, and the effective vertical stress path coefficient should also be -1.0, as described in Eq. (2.12). If the coefficient is less negative than -1.0, it means that the stress arching in the overburden and the sideburden resist the stress to be transferred. Also, the observed more negative value than -1.0 means the counter effect of the stress arching that tries to make a stress equilibrium. The observed normal distribution with a mean of -1.0 for the vertical stress path coefficient indicates that Eqs. (2.10) and (2.12) provides a reasonable estimate for the pore pressure response on vertical stresses of intra-reservoir faults, whereas bounding faults are slightly overestimated.

The spatial distribution plot of horizontal effective stress path coefficients γ_h' in Fig. 7c shows that the coefficients near the closed bounding faults and the injector are more negative ($-\gamma_h' > 0.3$) than

those in the southern reservoir ($-\gamma_h' < 0.3$), which has an open hydraulic boundary and experiences less change in pore pressure. This indicates that regions with larger pore pressure changes are more influenced by the boundaries. The peak of the histogram (Fig. 7d) also supports the observation that the boundary condition influences the coefficients. The bounding faults (VFZ, ØFC, northern bounding faults) have more negative values (-0.33 to -0.41) than the faults inside the reservoir ($\sim$ -0.32). The influence of the deformational boundary condition becomes more evident when comparing the effective horizontal stress paths assuming the uniaxial strain condition (calculated using Eq. (2.14) with a drained Poisson's ratio of 0.22, which is the same condition considered for the numerical model) to the calculated results. Fig. 7d shows that the uniaxial strain assumption ($\gamma_{h,uniaxial}' = -0.28$) underestimates the absolute value of the coefficients compared to the simulated field condition, which considered more realistic lateral deformation and associated stress changes. These results suggest that relying on the assumptions in
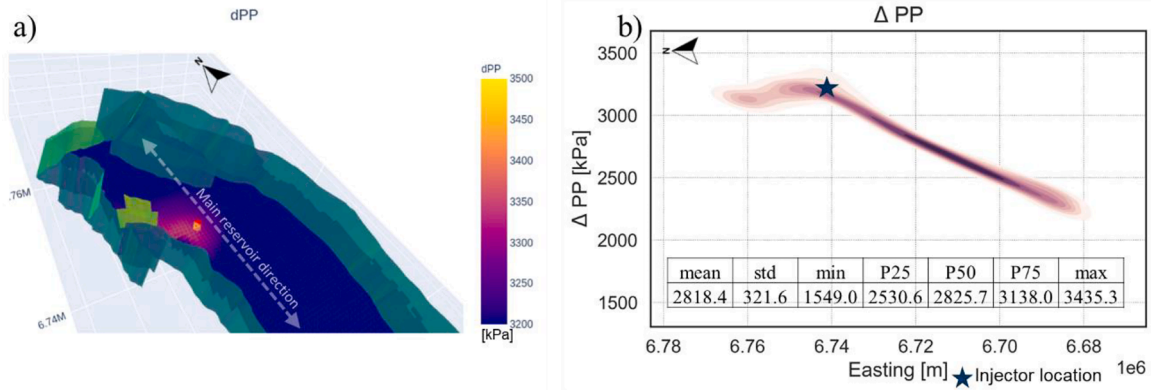
Fig. 5. a) Location of CO_2 injector (red dot) and pore pressure build-up after 25 years of injection, and b) pressure build along the main reservoir direction, which is approximately N.S. direction, together with statistics for the distribution.
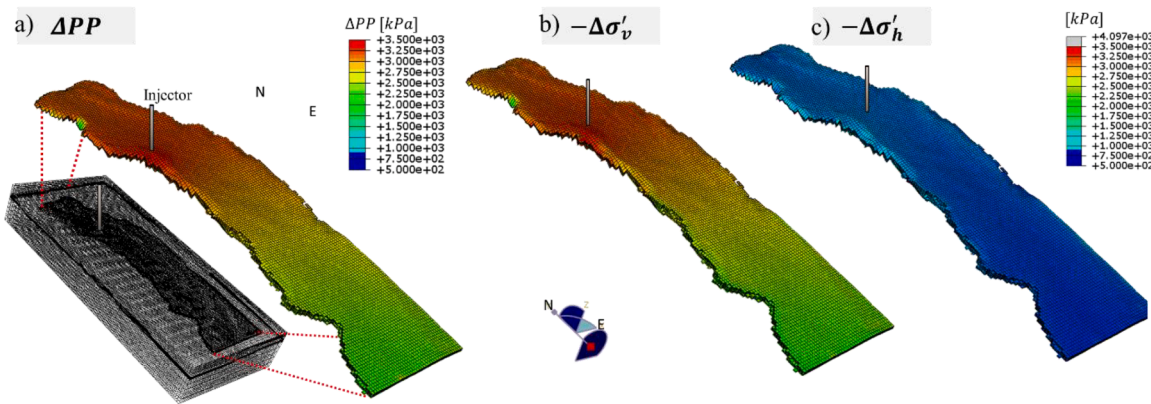
Fig. 6. Simulated CO_2 injection-induced stress change in the reservoir. a) 3D mesh of modelled Smeaheia area and implemented injection-induced pore pressure change in the reservoir domain. Figures b) and c) show the corresponding change of reservoir effective stresses after CO_2 injection for vertical effective stresses ($\Delta\sigma'_v$) and minimum horizontal effective stresses ($\Delta\sigma'_h$), respectively.

Eqs. (2.11) and (2.14) can result in errors when estimating the change in horizontal effective stresses. Assuming that change in horizontal effective stress change is equal to the pore pressure change (Eq. 2.11) can lead to a substantial overestimation of the effective horizontal stress change. Although the assumption with the uniaxial strain condition (Eq. 2.14) may better predict the field situation, particularly for the reservoir, it still does not provide an accurate estimation. The uniaxial strain condition tends to underestimate the effective horizontal stress change, especially for the bounding faults with significant changes in pore pressure, such as the Vette Fault Zone.

4.3. Stiffness sensitivity of the effective stress paths

The sensitivity of stiffness, particularly concerning heterogeneities and contrasts, on the stress paths and associated induced in-situ stress anisotropy and rotations are investigated using a series of 3D numerical simulations for the parametric cases outlined in Table 2. Fig. 8 presents a comparison of the calculated effective stress paths for the parametric cases. The results were statistically visualized in a bar chart with error bars and compared to the analytical estimation assuming the uniaxial strain condition, which is represented by red dotted lines. For the vertical effective stress path coefficients (Fig. 8a), the stiffness heterogeneities and contrasts rarely affect the estimated mean value for the intra-reservoir faults (i.e., the bar group IR in Fig. 8a). However, the error bars for the homogeneous reservoir domain (i.e. orange bar in Fig. 8a) show reduced spatial variation more than the heterogeneous base case (i.e. green bar in Fig. 8a). The bounding faults (i.e., the bar groups NB, VFZ,

ØFZ in Fig. 8a) show more variation in the estimated mean values than the intra-reservoir faults. Also, the variation is more affected by the stiffness contrast than the reservoir heterogeneity. The stiffness contrast results in around a maximum 20% variation of vertical effective stress paths for this study. For the horizontal effective stress path coefficients (Fig. 8b), we can see more drastic effects of the stiffness contrast on the bounding faults. When the surroundings are considered as soft material (i.e., case no. 2b in Table 2 and the yellow bars in Fig. 8b), the maximum value of +2 SD for the Vette Fault Zone is around $\gamma'_h = 0.64$, which is 127% higher than the uniaxial strain assumption (i.e., $-\gamma'_{h,uniaxial\ strain} = 0.282$). When the case with the soft surroundings is compared to the base case, the means of the bounding faults (i.e., $\gamma'_h = 0.42 - 0.49$) are around 20 per cent higher than that of the base cases (i.e., $\gamma'_h = 0.35$–0.41). The results of this parametric study indicate that the horizontal effective stress path coefficients can be significantly affected by stiffness contrast between the reservoir and surroundings, and using the uniaxial strain assumption can result in a change of the horizontal effective stress by less than half of the actual change from numerical simulation for the case where the surroundings are softer than the reservoir.

The simulation results also indicate that stiffness contrast caused by direction to the fault boundary (e.g. stiffness contrast caused by perpendicular vs. parallel to the faults) seems to result in anisotropy and rotation of in-situ stress condition. Fig. 8c presents that the initial isotropic effective horizontal stress condition becomes slightly anisotropic by $\sigma'_h / \sigma'_H = 5$–10% on average after the injection. Similar to
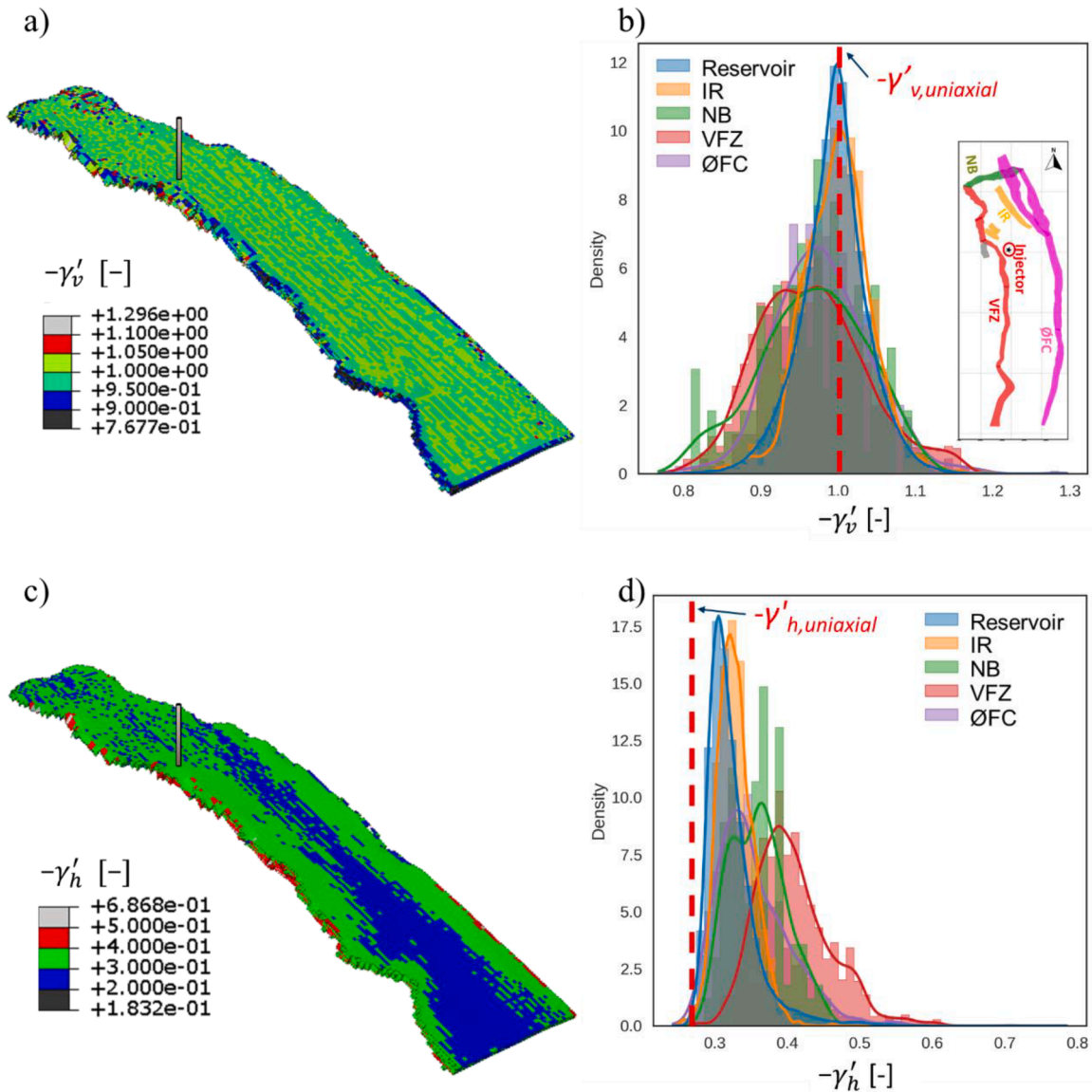
Fig. 7. Spatial distribution and statistical information for calculated vertical stresses path coefficients γ'_v (a and b) and horizontal effective stresses path coefficients γ'_h (c and d). Uniaxial strain conditions for vertical stress path coefficients ($\gamma'_{v,uniaxial} = -1.0$) and horizontal effective stress path coefficients ($\gamma'_{h,uniaxial} = -0.28$) are added as the red dashed lines in b) and d), respectively.

previously observed effects on the horizontal effective stress paths (seen in Fig. 8b), the bounding faults juxtaposed with soft sediments seem to experience more effective horizontal stress anisotropy σ'_h / σ'_H up to 20% compared to the reservoir with stiff surroundings. As consequence of stiffness contrast caused by direction to the fault boundary, near the bounding faults, the direction of the maximum horizontal stress σ_H becomes parallel to the faults (Fig. 8d).

4.4. Effect on fault stability assessments

The consequence of the difference in estimated stress path on fault stability assessment is evaluated using the conservative assumption of cohesionless faults ($C_0 = 0.0$ MPa, $\mu' = 0.6$) as the fault strength. Calculated allowable injection pressure Pc and the mobilized shear strength τ_{mob} for the cases assuming faults as a cohesionless material (Fig. 9) show that the uniaxial strain assumption overestimates the fault stability of most cases. Assuming stress paths to follow the uniaxial strain condition, the Pc and the τ_{mob} were calculated as 1.74 MPa and 0.65, respectively. When the mean of numerically calculated stress paths

is applied to the simulation, the calculated Pc and the τ_{mob} are 0.74 – 1.56 MPa and 0.69 – 0.83, respectively, significantly lower than the uniaxial strain assumption. Especially for the bounding faults, when the surrounding material is softer than the reservoir, the numerical simulation model results in the instability of critically stressed faults. The calculated Pc is less than zero, and the τ_{mob} is higher than one. Utilizing the uniaxial strain assumption gives too optimistic results and cannot capture the more critical scenarios, including a failure for the critically oriented faults. These results clearly indicate that using the uniaxial strain assumption for the bounding fault is less representative than in the reservoir.

The overestimation of the fault stability when using the uniaxial strain condition can also be seen in other parametric studies, including those with high-end fault strengths assuming the same as that in intact reservoir rock ($C_0 = 5$ MPa, $\mu' = 0.27$), that consider the variation of the strength and fault geometries. Comparison of mobilized shear strengths and the associated overestimated stability when using the uniaxial assumption ($\tau_{mob,numerical\ model} / \tau_{mob,uniaxial}$) are plotted in Fig. 10. The bar chart of calculated mobilized shear strength (Fig. 10a) presents that the
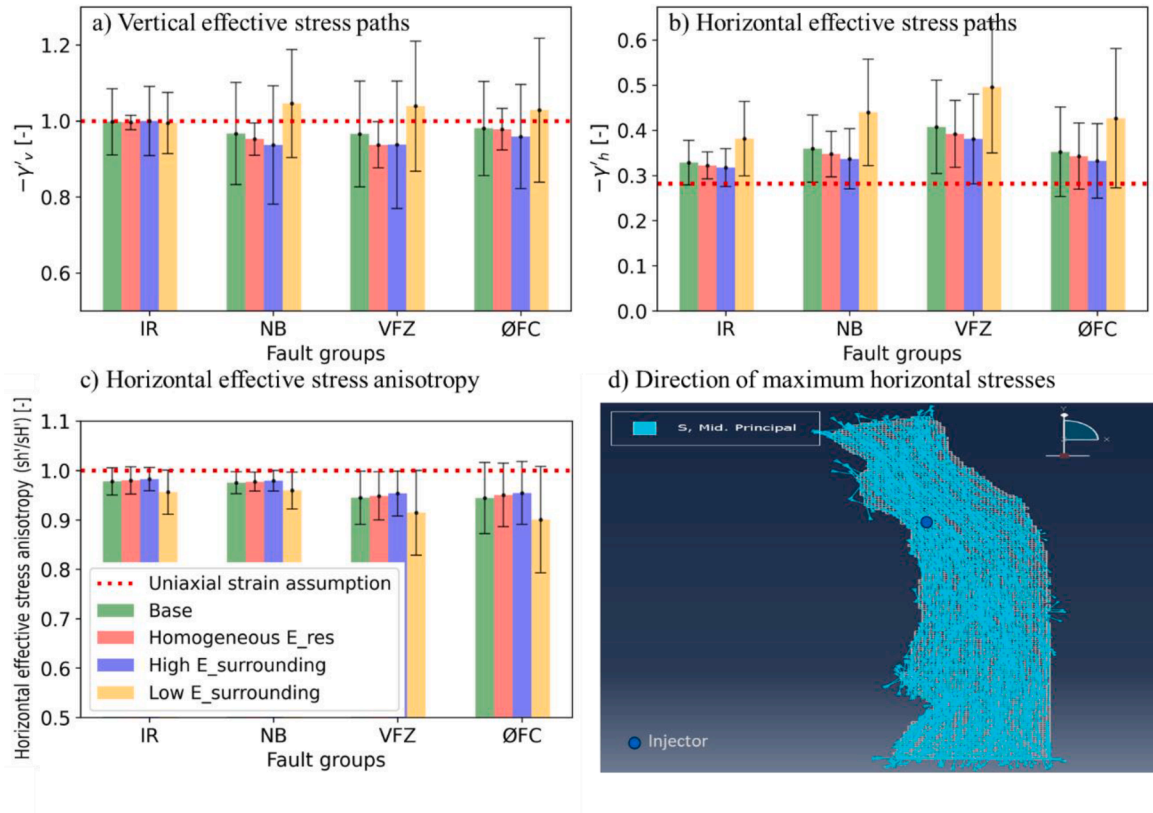
Fig. 8. Comparison of reservoir stiffness heterogeneity and contrast effects on a) vertical effective stress paths, b) vertical effective stress paths, and c) horizontal effective stress anisotropy. The error bars indicate the ± 2 **SD** of the calculated stress path coefficients. The directions of maximum horizontal stresses after the injection are plotted in figure d).
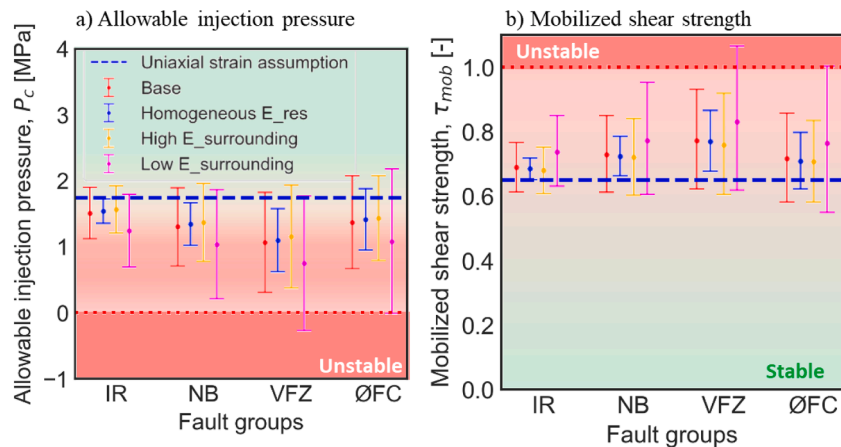
Fig. 9. Results of fault stability assessment using conservative strength assumption of a cohesionless material ($C_0 = 0.0$ MPa, $\mu' = 0.6$). The stability values are presented as a) allowable injection pressure and b) mobilized shear strengths.

case of high fault strength (i.e. high cohesion D:60° S:169°) results in stable fault condition even after the injection with the mobilized shear strengths of around 0.3 to 0.4, and the variation of calculated mobilized shear strength is smaller than in the cohesionless case. However, when the calculated mobilized shear strength is normalized by the results using the uniaxial strain condition ($\tau_{mob,numerical\ model}/\tau_{mob,uniaxial}$), the associated overestimated stability (Fig. 10b) is almost the same as that of the cohesionless case. When the dip and strike are assumed to be similar to the Vette Fault Zone (i.e., D: 60° S: 169°), the overestimated stability caused by the uniaxial strain conditions is around 35–60%. For the less critically orientated faults (i.e., cohesionless D: 42° S: 169°), the stability

variation, expressed as the length of the error bars, is less than the critically orientated case.

Fig. 10 also shows the effect of injection-induced stress anisotropy and associated consequences on the fault stability in different directions. The fault perpendicular to the major bounding faults (i.e. cohesionless D: 60° S: 252°) shows slightly more stable fault conditions but higher stability variation than the base case. The stress paths of parametric end members (Fig. 11) can help us understand why faults perpendicular to the major bounding faults become more stable than the bounding faults, even though the field initially has isotropic horizontal stress conditions. As illustrated in Fig. 8d, injection leads to a slight anisotropy in
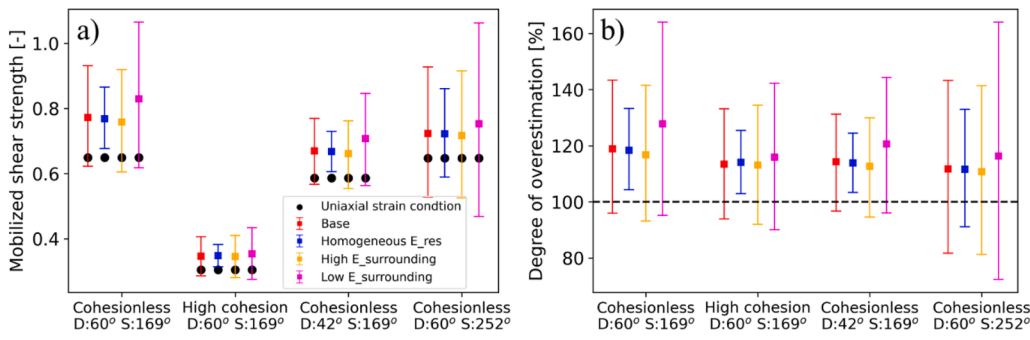
Fig. 10. Effect of strength and fault geometry – dip (D) and strike (S) – variation on a) the mobilized shear strengths and b) the associated over-estimated stability using the uniaxial strain assumption. The rectangle boxes and error bars represent stability values with mean and ± 2 **SD** of the calculated stress path coefficients, respectively. The strengths used in the Cohesionless and High cohesion cases correspond to the low-end ($C_0 = 0.0$ MPa, $\mu' = 0.6$) and high-end assumption ($C_0 = 5$ MPa, $\mu' = 0.27$) for fault strengths, respectively.
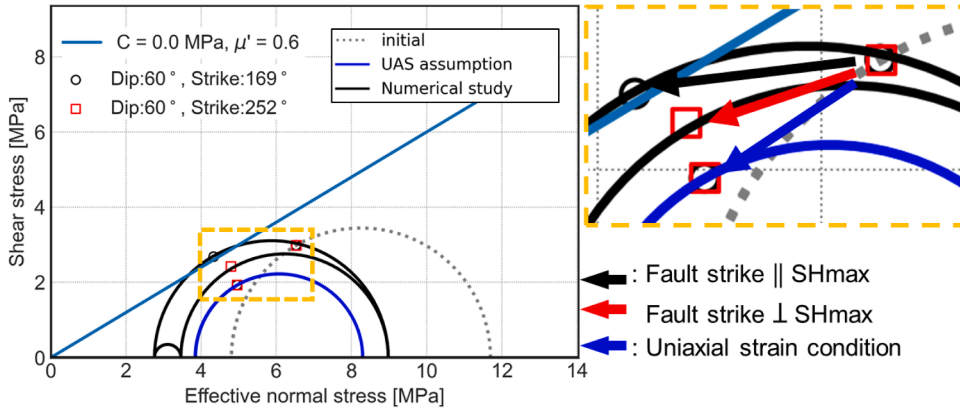
Fig. 11. Mohr circle representations of injection-induced stress anisotropy and associated consequence on stress paths in different fault directions. In the figure left, the black and blue solid lines are the injection-induced stress conditions calculated using the numerical simulation and the uniaxial strain (UAS) assumption, respectively. The dotted line is initial stress condition, which initially had an isotropic horizontal stress conditions. Zoomed figure in right shows associated stress paths in different fault strikes.

horizontal stresses and rotates the maximum stress directions parallel to its major bounding faults. The results of the numerical study plotted in Fig. 11 also show the injection-induced stress anisotropy by displaying a difference between the minimum and maximum horizontal stresses after the injection, even though they were the same before the injection. As a consequence of this stress anisotropy and stress rotation, faults perpendicular to S_{Hmax} experience a more decrease in shear stress than those parallel to S_{Hmax}, and resulting in more stable conditions. This explains why faults perpendicular to σ_H are more stable than those parallel to σ_H. However, the stability of faults perpendicular to σ_H orientation is not only influenced by σ_h and σ_v (or minimum and maximum principal stresses) but also by the variation of intermediate principal stress σ_H. As a result, faults orientated perpendicularly to σ_H appear to have higher variation in the stability assessment results than the base case, due to additional uncertainties caused by injection-induced horizontal stress anisotropy.
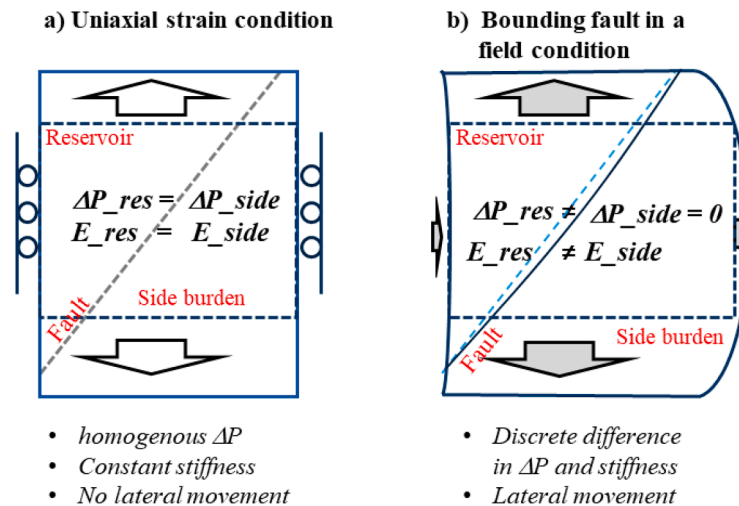
5. Discussion

5.1. Underestimated effective horizontal stress change in simplified uniaxial strain assumption

Our results show that when using the uniaxial strain assumption, only the lower bound of the effective stress change in the horizontal direction is captured (Fig. 7d). Stress change is larger for the bounding faults subjected to a significant change in pore pressure (e.g., VFZ) than for the homogeneous pore pressure distribution within the reservoir. Observations also highlight that the uniaxial strain condition leads to a more discrepancy in the estimated stress change and stability when reservoir surrounding material, including faults, is softer than the reservoir (Fig. 9). These observed differences can be explained mainly by the assumptions regarding lateral deformation around the faults. The uniaxial strain condition assumes no lateral movement, and the total horizontal stress will then increase according to poroelastic equations,

and the resulting change in effective horizontal stress due to pore pressure increase will be less (i.e. increasing $\Delta\sigma_h$ will counteract ΔPP in the expression of effective stress, $\Delta\sigma'_h = \Delta\sigma_h - \Delta PP$). When the material is allowed to deform laterally on the fault/reservoir boundary as modelled in the 3D model, such build-up of total horizontal stress will be less and absorbed in the deforming rock, and the resulting change in effective horizontal stress induced by pore pressure will be more significant. Moreover, the softer the surrounding boundary material, the more of the total stress change will instead be absorbed into strains. Intra-reservoir faults within an assumed homogeneous domain with a homogeneous pore pressure build-up on each side of the fault (Fig. 12a) will experience negligible lateral displacement due to lateral confinement. The conditions are thus suitable for applying the uniaxial strain assumptions. However, for the bounding faults (Fig. 12b), in-homogeneity in both pore pressure and stiffness is expected between the reservoir and the side burden. This results in imbalanced confinement near the faults and lateral deformation rather than increasing the total stress. The observed injection-induced horizontal stress anisotropy (Fig. 8c) is explained by the directional difference in stiffness contrast along faults that form a boundary in mechanical stiffness. Increased injection-induced horizontal stress anisotropy is observed along the N-S trending bounding faults compared to the intra-reservoir faults (Fig. 8c). The maximum principal stress (S_{Hmax}) rotates near the bounding faults and becomes parallel to the N-S trending bounding faults. Field-measured stress conditions derived from leak-off tests and density logs from hydrocarbon production fields like Ekofisk (Hettema et al., 2000) and Groningen fields (Teufel et al., 1991) also show that the lab-measured uniaxial strain condition underestimates the field-measured effective horizontal stresses changes. It also supports that the uniaxial strain assumption should be used as a low estimate of horizontal effective stress change of bounding faults when the injection-induced fault stress changes are estimated using an analytical solution.

Our work highlights mechanical contrasts in the stiffness properties

a) Uniaxial strain condition

$\Delta P\_res = \Delta P\_side$
$E\_res = E\_side$

Reservoir

Side burden

Fault

- *homogenous ΔP*
- *Constant stiffness*
- *No lateral movement*

b) Bounding fault in a field condition

$\Delta P\_res \neq \Delta P\_side = 0$
$E\_res \neq E\_side$

Reservoir

Side burden

Fault

- *Discrete difference in ΔP and stiffness*
- *Lateral movement*

Fig. 12. Illustrative description of the difference in boundary, pore pressure, and stiffness condition between a) uniaxial strain conditions assuming no lateral movement and b) field conditions for a deforming bounding fault.

on each side of a bounding fault as the controlling parameter for the stress path for the fault, suggesting that faults displacing the stratigraphy and juxtaposition material of high mechanical contrast need a detailed evaluation of the stress path. One of the limitations of our study is that faults are not modelled as discrete fault structures, but we assumed the same material as the surroundings. This simplification is inspired and supported by findings from a detailed fault study for depletion in the Statfjord field (Cuisiat et al., 2010), concluding that the stability of faults is not sensitive to stiffness distributions of the fault itself, including geometrical variations and uncertainties, because the behaviour of a relatively thin domain can be mostly governed by surrounding materials. However, with the current methodology for quantification of sensitivity, we see it might be valuable to include variation in the local fault stiffness and thickness on the fault stress paths as well as the effect of relative fault offset to its horizons in future studies. Recent studies investigating the effect of fault offset on stability (Jansen et al., 2019; van den Bogert and van Eijs, 2020; van den Hoek and Poessé, 2021; H. Wu et al., 2021) show that the stability overestimation is related to geometrical effects and suggest including top reservoir surface rugosity and gradients as parameters influencing fault stability. In addition, it is worth noting that the stress path of faults can also be affected by other aspects, including thermo- (e.g., thermal cooling) and hydro- (e.g., un-drained or partial drainage in a fault) behaviour, the material hetero-geneities and uncertainties caused by the simplification of non-linear material behaviours, geometrical aspects, and other operational condi-tion (e.g., injection vs depletion, injection rates and associated hetero-geneity in pressure build-up). A comprehensive sensitivity study under generalized geometry and parameter conditions may thus be helpful in ranking the relative importance of factors affecting the uncertainties in stress paths and associated stability evaluation. While the mobilized shear strength criterion used in this study provides an absolute measure of fault stability, it does not capture changes in shear risk over time or relative changes in fault stability. An indicator that can show stress path directions relative to the shear envelope, such as the Coulomb Failure Stress change (King et al., 1994), would improve further insights. Then, our findings, which highlight quantifying the stability overestimation of the uniaxial strain condition, can be more practically used to calibrate the preliminary results of fault stability that have to be carried out using the analytical stress path assumptions in an early stage of the CO_2 storage field development.

5.2. Applicability of simplified analytical approaches to norwegian continental shelf CO_2 storage, including the horda platform

Uncertainties and limitations in stress path assumptions for faults outlined in this paper provide valuable input for the use of simplified analytical fault stability calculations in an early screening phase of a project. In more mature projects with detailed geological models and mechanical data available, the need for detailed geomechanical modelling may be justified based on the geological setting and expected stiffness contrasts along faults.

The current findings may provide practical guidelines for how much correction is needed on the resulting stability when the uniaxial strain condition is assumed in the analytical solution for fault stability evalu-ation. Our study shows that uniaxial strain conditions tend to over-estimate the fault stability (i.e., lowering mobilized shear strengths or a slip tendency) by 20–30% on average compared to the numerical model (Fig. 10b). The degree of overestimation appears to be less affected by the strength properties, including the variation friction angle. This can be relevant to the attribute of the Mohr coulomb criteria, in which the shear strength changes proportionally with the effective stress change. Further, good knowledge of the stiffness contrast between the reservoir and surrounding units is necessary when suggesting how much correc-tion is needed for a reservoir-bounding fault. When the surrounding material is composed of stiffer or softer material compared to the reservoir, the overestimated stability can be up to 40 and 60%, respec-tively. Where the Vette Fault Zone juxtaposes the reservoir with the Draupne Formation, a stiffness of 5.56 GPa is used for the reservoir and 5 GPa is used for the surroundings in the base case and 2 GPa in the low stiffness case (Table 2). This is in line with the stiffness measured for Draupne Formation in the Ling Depression, ranging from 2.5 to 5.0 GPa (Mondol, 2019; Soldal et al., 2021). However, the Øygarden Fault Complex juxtaposes the reservoir with the basement composed of Pre-cambrian granite (L. Wu et al., 2021). The stiffness of the actual base-ment rock is not known, but it is expected to be stiffer compared to the reservoir. Hence, the correction factor needed for the stress path can be smaller for the ØFC than for the VFZ (i.e. 40% vs 60%). In general, for the North Sea settings in a normal faulting stress regime, we suggest the mobilized shear strengths (or slip tendency) can be corrected by increasing the change of effective horizontal stress by 30% for the base case conditions, and 40 to 60% for the conservative case outlined above. This may be less conservative than the assumption without considering the poroelastic effect (Eq. (2.11)) but more realistic than the uniaxial strain assumption. If the fault geometry is critically orientated and fault cohesion is very low, such a correction can be less straightforward, and

uniaxial strain assumption is then not recommended for the screening assessment.

It should be noted that the assumptions used in the model, particularly the assumptions of constant reservoir Poisson's ratio and the closed hydraulic boundary conditions of the bounding faults and surroundings, could impact the stability results. Our conclusion depends entirely on the assumption that the reservoir's lateral ends are closed faults. However, recent publications (Lothe et al., 2019; Mulrooney et al., 2020) have addressed that the bounding faults in the Smeaheia area could be classified as an open boundary based on observable Troll depletion effects. If the field condition is closer to open faults with little throw and negligible pore pressure differential over them, the results more closely align with the uniaxial strain estimations, as observed in the results for Reservoir and IR in Fig. 7. This study also assumed a Biot coefficient equal to 1. However, if these stiffnesses were larger, which might be justified given the full elastic unloading conditions that potentially pertain, the Biot coefficient would become significant. A low Biot coefficient can potentially underestimate the change in effective horizontal stresses, leading to a further overestimation of the stability value, as described in Eq. (2.13). Moreover, it is important to acknowledge that the site-specific conditions used in this study may differ from those used by the relevant operators, who likely possess more detailed and comprehensive information about the area's characteristics. Thus, it is crucial to avoid drawing critical conclusions based solely on the results of this study, which rely on critical assumptions such as the ones mentioned above. Such conclusions may mislead the site stability and should be avoided.

6. Conclusion

In this study, we compared the simplified uniaxial strain assumption and 3D geomechanics numerical simulations for fault stress paths to quantify uncertainties in fault stability assessment for CO_2 storage. Using the Smeaheia case study in the Horda Platform, we simulated the 3D distribution of CO_2 injection-induced stress change induced by pore pressure increase. We found that the uniaxial strain assumption corresponds to the low bound of the effective stress change in the horizontal direction, leading to discrepancies in stress estimation and stability assessment results (e.g., allowable injection pressure, mobilized shear strengths), particularly when the bounding fault is juxtaposed with a softer material than the reservoir.

In terms of the stability assessment, our study shows that using uniaxial strain conditions in the analytical solution tends to overestimate the stability (i.e., mobilized shear strengths or a slip tendency) by 20 – 30% on average and up to 60% for the extreme cases when the bounding fault is juxtaposed with a softer material than the reservoir. This study confirms that the uniaxial strain assumption in the analytical model does not capture critical scenarios for fault stability assessments, and we recommend corrections to account for these limitations.

We also highlight the limitations of applying these corrections in practice, emphasizing the need for further research on the site-specific conditions, including the effects of realistic hydraulic boundary conditions and material heterogeneity, to better understand the implications of these findings in various geological settings and conditions.

CRediT authorship contribution statement

Jung Chan Choi: Conceptualization, Methodology, Data curation, Writing – original draft. **Elin Skurtveit:** Conceptualization, Data curation, Writing – original draft, Funding acquisition. **Khoa D.V. Huynh:** Conceptualization, Methodology, Writing – review & editing. **Lars Grande:** Conceptualization, Data curation, Writing – review & editing.

Declaration of Competing Interest

The authors declare that they have no known competing financial

interests or personal relationships that could have appeared to influence the work reported in this paper.

Data availability

The authors do not have permission to share data.

References

Andrews, J., Fintland, T., Helstrup, O., Horsrud, P., Raaen, A., 2016. Use of unique database of good quality stress data to investigate theories of fracture initiation, fracture propagation and the stress state in the subsurface.

Andrews, J.S., de Lesquen, C., 2019. Stress determination from logs. Why the simple uniaxial strain model is physically flawed but still gives relatively good matches to high quality stress measurements performed on several fields offshore Norway. In: Presented at the 53rd U.S. Rock Mechanics/Geomechanics Symposium. American Rock Mechanics Association.

Barton, N., Bandis, S., 1991. Review of predictive capabilities of JRC-JCS model in engineering practice. Publikasjon - Norges Geotekniske Institutt 182, 1–8.

Bjørnarå, T.I., Mathias, S.A., Nordbotten, J.M., Park, J., Bohloli, B., 2014. Capturing the coupled hydro-mechanical processes occurring during CO2 injection – example from In Salah. In: Energy Procedia, 12th International Conference on Greenhouse Gas Control Technologies, GHGT-12, 63, pp. 3416–3424. https://doi.org/10.1016/j.egypro.2014.11.370.

Bretan, P., Yielding, G., Mathiassen, O.M., Thorsnes, T., 2011. Fault-seal analysis for CO $_2$ storage: an example from the Troll area, Norwegian Continental Shelf. Petrol. Geosci. 17, 181–192. https://doi.org/10.1144/1354-079310-025.

Ching, J., Phoon, K.-.K., 2013. Mobilized shear strength of spatially variable soils under simple stress states. Struct. Safety 41, 20–28. https://doi.org/10.1016/j.strusafe.2012.10.001.

Choi, J.C., Skurtveit, E., Grande, L., Park, J., 2019. Effect of CO2 Injection-Induced Stress Rotation On the Fault Stability and Induced Seismicity in overburden: Numerical investigation. Presented at the TCCS-10, Trondheim, Norway.

Cuisiat, F., Jostad, H.P., Andresen, L., Skurtveit, E., Skomedal, E., Hettema, M., Lyslo, K., 2010. Geomechanical integrity of sealing faults during depressurisation of the Statfjord Field. J Struct Geol 32, 1754–1767. https://doi.org/10.1016/j.jsg.2010.01.006.

Dassault Systèmes Simulia Corp, 2017. ABAQUS/Standard User's Manual, Version 2017. Dassault Systèmes Simulia Corp, United States.

Detournay, E., Cheng, A.H.-D., 1988. Poroelastic response of a borehole in a non-hydrostatic stress field. Int. J. Rock Mechan. Mining Sci. Geomechan. Abstracts 25, 171–182. https://doi.org/10.1016/0148-9062(88)92299-1.

Fjær, E., Holt, R.M., Raaen, A.M., Risnes, R., Horsrud, P., 2008. Petroleum Related Rock Mechanics, 2nd Edition. Elsevier.

Fossen, H., Khani, H.F., Faleide, J.I., Ksienzyk, A.K., Dunlap, W.J., 2017. Post-Caledonian extension in the West Norway–northern North sea region: the role of structural inheritance. SP 439, 465–486. https://doi.org/10.1144/SP439.6.

Gassnova, 2013. Troll kystnaer subsurface evaluation report.

Gassnova, 2021. Smeaheia CO2 storage prospect reference dataset. 10.11582/2021.00012.

Grande, L., Griffith, L., Park, J., Choi, J.C., Bjørnarå, T., Sauvin, G., Mondol, N., 2020. Acoustic emission testing of shales for evaluation of microseismic monitoring of north sea CO2 storage sites. In: EAGE 2020 Annual Conference & Exhibition Online. Presented at the EAGE 2020 Annual Conference & Exhibition Online. European Association of Geoscientists & Engineers, pp. 1–5. https://doi.org/10.3997/2214-4609.202011984. Online, pp.

Gueguen, Y., Bouteca, M., 1999. Mechanical properties of rocks: pore pressure and scale effects. Oil Gas Sci. Technol. - Rev. IFP 54, 703–714. https://doi.org/10.2516/ogst:1999060.

Hettema, M., Papamichos, E., Schutjens, P., 2002. Subsidence delay: field observations and analysis. Oil Gas Sci. Technol. - Rev. IFP 57, 443–458. https://doi.org/10.2516/ogst:2002029.

Hettema, M.H.H., Schutjens, P., Verboom, B.J.M., Gussinklo, H.J., 2000. Production-induced compaction of a sandstone reservoir: the strong influence of stress path. SPE Reserv. Evaluation Engin. 3, 342–347.

Horstad, I., Larter, S.R., 1997. Petroleum Migration, Alteration, and Remigration Within Troll Field. Norwegian North Sea. Bulletin 81 (1997). https://doi.org/10.1306/522B42F3-1727-11D7-8645000102C1865D.

Jansen, J.D., Singhal, P., Vossepoel, F.C., 2019. Insights from closed-form expressions for injection- and production-induced stresses in displaced faults. J. Geophys. Res. Solid Earth 124, 7193–7212. https://doi.org/10.1029/2019JB017932.

King, G., Stein, R., Lin, J., 1994. Static stress changes and the triggering of earthquakes. Bull. - Seismol. Society Am. 84.

Lothe, A.E., Bergmo, P.E.S., Emmel, B., Eliasson, P., 2019. Effects of uncertainties in fault interpretations on pressure depletion and CO2 storage injection at horda platform, offshore Norway. 10.2139/ssrn.3366363.

Marone, C., 1995. Fault zone strength and failure criteria. Geophys. Res. Lett. 723–726.

Mesri, G., Shahien, M., 2003. Residual Shear strength mobilized in first-time slope failures. J. Geotech. Geoenviron. Engin. 129, 12–31. https://doi.org/10.1061/(ASCE)1090-0241(2003)129:1(12).

Michie, E.A.H., Mulrooney, M.J., Braathen, A., 2021. Fault interpretation uncertainties using seismic data, and the effects on fault seal analysis: a case study from the Horda Platform, with implications for CO2 storage. Solid Earth 12, 1259–1286. https://doi.org/10.5194/se-12-1259-2021.

Mondol, N.H., 2019. Geomechanical and Seismic Behaviors of Draupne Shale: a Case Study from the Central North Sea. In: 81st EAGE Conference and Exhibition 2019. Presented at the 81st EAGE Conference and Exhibition 2019. European Association of Geoscientists & Engineers, London, UK, pp. 1–5. https://doi.org/10.3997/2214-4609.201901599.

Morita, N., Whitfill, D.L., Nygaard, O., Bale, A., 1989. A quick method to determine subsidence, reservoir compaction, and in-situ stress induced by reservoir depletion. J. Petrol. Technol. 41, 71–79. https://doi.org/10.2118/17150-PA.

Morris, A., Ferrill, D.A., Henderson, D.B., 1996. Slip-tendency analysis and fault reactivation. Geology 24, 275–278. https://doi.org/10.1130/0091-7613(1996)024<0275:STAAFR>2.3.CO;2.

Mulrooney, M.J., Osmond, J.L., Skurtveit, E., Faleide, J.I., Braathen, A., 2020. Structural analysis of the Smeaheia fault block, a potential CO2 storage site, northern Horda Platform, North Sea. Mar. Pet. Geol. 121, 104598 https://doi.org/10.1016/j.marpetgeo.2020.104598.

Osmond, J., Mulrooney, M.J., Holden, N., Skurtveit, E., Faleide, J.I., Braathen, A., 2022. Structural traps and seals for expanding CO2 storage in the northern Horda platform, North Sea. Am. Assoc. Pet. Geol. Bull. 0 https://doi.org/10.1306/03222221110.

Park, J., Griffiths, L., Dautriat, J., Grande, L., Rodriguez, I.V., Iranpour, K., Bjørnarå, T.I., Moreno, H.M., Mondol, N.H., Sauvin, G., Sarout, J., Soldal, M., Oye, V., Dewhurst, D.N., Choi, J.C., Best, A.I., 2022. Induced-seismicity geomechanics for controlled CO2 storage in the North Sea (IGCCS). Int. J. Greenhouse Gas Control 115, 103614. https://doi.org/10.1016/j.ijggc.2022.103614.

Rahman, M.J., Choi, J.C., Fawad, M., Mondol, N.H., 2021. Probabilistic analysis of Vette fault stability in potential CO2 storage site Smeaheia, offshore Norway. Int. J. Greenhouse Gas Control 108, 103315. https://doi.org/10.1016/j.ijggc.2021.103315.

Rahman, M.J., Fawad, M., Choi, J.C., Mondol, N.H., 2022. Effect of overburden spatial variability on field-scale geomechanical modeling of potential CO2 storage site Smeaheia, offshore Norway. J. Nat. Gas Sci. Eng. 99, 104453 https://doi.org/10.1016/j.jngse.2022.104453.

Rice, J.R., Rice, J.R., 1977. Pore pressure effects in inelastic constitutive formulations for fissured rock masses. Advances in Civil Engineering Through Engineering Mechanics. ASCE., New York, NY, pp. 360–363. . :Advances in Civil Engineering through Engineering Mechanics360–363.

Rudnicki, J.W., 1999. Alteration of regional stress by reservoirs and other inhomogeneities: stabilizing or destabilizing?. In: Presented at the Proc. 9th Intern., Congress Rock Mech. Paris, France, 3, pp. 25–28. August.

Rutqvist, J., 2012. The geomechanics of CO2 storage in deep sedimentary formations. Geotech. Geol. Eng. 30, 525–551. https://doi.org/10.1007/s10706-011-9491-0.

Rutqvist, J., Birkholzer, J., Cappa, F., Tsang, C.-.F., 2007. Estimating maximum sustainable injection pressure during geological sequestration of CO2 using coupled fluid flow and geomechanical fault-slip analysis. In: Energy Conversion and Management, Geologic Carbon Sequestration and Methane Hydrates Research from

the TOUGH Symposium 2006, 48, pp. 1798–1807. https://doi.org/10.1016/j.enconman.2007.01.021.

Rutqvist, J., Rinaldi, A.P., Cappa, F., Moridis, G.J., 2013. Modeling of fault reactivation and induced seismicity during hydraulic fracturing of shale-gas reservoirs. J. Pet. Sci. Eng. 107, 31–44. https://doi.org/10.1016/j.petrol.2013.04.023.

Skurtveit, E., Aker, E., Soldal, M., Angeli, M., Wang, Z., 2012. Experimental investigation of CO2 breakthrough and flow mechanisms in shale. Pet. Geosci. 18, 3–15. https://doi.org/10.1144/1354-079311-016.

Skurtveit, E., Choi, J.C., Osmond, J., Mulrooney, M., Braathen, A., 2018. 3D fault integrity screening for smeaheia CO2 injection site. In: 14th Greenhouse Gas Control Technologies Conference Melbourne, pp. 21–26.

Soldal, M., Skurtveit, E., Choi, J.C., 2021. Laboratory Evaluation of mechanical properties of draupne shale relevant for CO2 seal integrity. Geosciences (Basel) 11, 244. https://doi.org/10.3390/geosciences11060244.

Soltanzadeh, H., Hawkes, C.D., 2008. Semi-analytical models for stress change and fault reactivation induced by reservoir production and injection. J. Pet. Sci. Eng. 60, 71–85. https://doi.org/10.1016/j.petrol.2007.05.006.

Søreide, O.K., Hansen, S., Stenebråten, 2014. Estimation of reservoir stress effects due to injection of cold fluids: an example from NCS. In: Presented at the 48th U.S. Rock Mechanics/Geomechanics Symposium. OnePetro.

Streit, J.E., Hillis, R.R., 2004. Estimating fault stability and sustainable fluid pressures for underground storage of CO2 in porous rock. Energy 29, 1445–1456. https://doi.org/10.1016/j.energy.2004.03.078.

Suvorov, A.P., Selvadurai, A.P.S., 2019. The Biot coefficient for an elasto-plastic material. Int. J. Eng. Sci. 145, 103166 https://doi.org/10.1016/j.ijengsci.2019.103166.

Terzaghi, K., 1943. Theoretical Soil Mechanics. John Wiley & Sons, Inc., New York.

Thompson, N., Andrews, J.S., Bjørnarå, T.I., 2021. Assessing potential thermo-mechanical impacts on caprock due to co2 injection—a case study from northern lights CCS. Energies 14, 5054. https://doi.org/10.3390/en14165054.

Thompson, N., Andrews, J.S., Wu, L., Meneguolo, R., 2022. Characterization of the in-situ stress on the Horda platform – a study from the Northern lights Eos well. Int. J. Greenhouse Gas Control 114, 103580. https://doi.org/10.1016/j.ijggc.2022.103580.

Teufel, L.W., Rhett, D.W., Farrell, H.E., 1991. Effect of reservoir depletion and pore pressure drawdown on in situ stress and deformation in the ekofisk field, North Sea. Presented at the 32nd U.S. Symposium on Rock Mechanics (USRMS), p. ARMA-91-063.

van den Bogert, P.A.J., van Eijs, R.M.H.E., 2020. Why Mohr-circle analyses may underestimate the risk of fault reactivation in depleting reservoirs. Int. J. Rock Mech. Min. Sci. 136, 104502 https://doi.org/10.1016/j.ijrmms.2020.104502.

van den Hoek, P.J., Poessé, J.W., 2021. Assessment of Seismic Risk in Geothermal and Hydrocarbon Reservoirs Using an Exact Analytical Solution of Stress Change. In: Presented at the SPE Europec featured at 82nd EAGE Conference and Exhibition. OnePetro. https://doi.org/10.2118/205122-MS.

Wiprut, D., Zoback, M.D., 2002. Fault reactivation, leakage potential, and hydrocarbon column heights in the northern north sea. In: Koestler, Andreas G., Hunsdale, Robert (Eds.), Norwegian Petroleum Society Special Publications, Hydrocarbon Seal Quantification Norwegian Petroleum Society Conference. Elsevier, pp. 203–219.

Wong, R.C.K., Ma, S.K.Y., Wong, R.H.C., Chau, K.T., 2007. Shear strength components of concrete under direct shearing. Cem. Concr. Res. 37, 1248–1256. https://doi.org/10.1016/j.cemconres.2007.02.021.

Wu, H., Vilarrasa, V., De Simone, S., Saaltink, M., Parisio, F., 2021. Analytical solution to assess the induced seismicity potential of faults in pressurized and depleted reservoirs. J. Geophys. Res. 126, e2020JB020436 https://doi.org/10.1029/2020JB020436.

Wu, L., Thorsen, R., Ottesen, S., Meneguolo, R., Hartvedt, K., Ringrose, P., Nazarian, B., 2021. Significance of fault seal in assessing CO2 storage capacity and containment risks – an example from the Horda Platform, northern North Sea. Pet. Geosci. 27, petgeo2020. https://doi.org/10.1144/petgeo2020-102.